

Measuring accretion impact radii with optical and gravitational wave observations of compact binaries

Eric Addison

Department of Physics, Utah State University, Logan, Utah 84322

Katelyn Breivik

Center for Interdisciplinary Exploration and Research in Astrophysics (CIERA) & Department of Physics and Astronomy, Northwestern University, Evanston, IL 60208

Shane L. Larson

Center for Interdisciplinary Exploration and Research in Astrophysics (CIERA) & Department of Physics and Astronomy, Northwestern University, Evanston, IL 60208
Department of Physics, Utah State University, Logan, Utah 84322

ABSTRACT

One of the primary astrophysical sources for space-based gravitational wave observatories will be ultra-compact binary star systems in the Milky Way. Of the millions of such systems in the galaxy, several thousand will be individually resolvable to a spaceborne gravitational wave observatory. For a large number of these systems, multi-messenger observing campaigns with both gravitational wave and electromagnetic telescopes will be possible. The multi-messenger characterization of compact binaries provides a useful synergy of observing capabilities that can be exploited to recover detailed information about the underlying astrophysical processes in the binary. This paper discusses how simultaneous photon and gravitational wave observations of mass transferring binaries can be used to characterize the accretion disks around the primary. The results suggest that for a large number of systems at a variety of inclinations, accretion disk radii can be measured to a precision of better than 5%. This is comparable to measurements using electromagnetic observations of eclipsing systems, but is important because it will work for a much wider range of binary inclination angles, including non-eclipsing systems.

Subject headings: PICK SOME KEYWORDS

1. Introduction

The interface between astrophysics and gravitational wave astronomy is an important, emerging area of research as new methods of analyzing and correlating gravitational data with traditional electromagnetic data are found. Of particular interest are ultra-compact binary stars in the Milky Way galaxy. Population estimates based on observed local space densities (Hils et al. 1990; Timpano et al. 2006) as well as population synthesis calculations (Nelemans et al. 2001b,a; Belczyn-

ski et al. 2008) suggest that all told, the Milky Way may be populated by as many as 10^7 ultra-compact binaries. This population will be dominated by white dwarf systems, with fewer numbers of systems where at least one component is a neutron star or stellar mass black hole.

The ultra-compact binaries are characterized by strongly bound components (often mass transferring, or having evolved to their current state through significant periods of mass transfer) and short orbital periods. Binaries with orbital periods

of $P_{orb} \sim 10^5$ s to $P_{orb} \sim 1$ s should be easily observable in the gravitational wave spectrum by any future space-based observatory. The archetype of such detectors has been the Laser Interferometer Space Antenna (LISA) (Bender 1998); current design concepts include the European eLISA-NGO (Amaro-Seoane et al. 2013a), and the US SGO (Amaro-Seoane et al. 2013b; Livas 2012; Stebbins 2012) designs.

The sheer numbers of ultra-compact binary systems are expected to produce a confusion-limited foreground of gravitational waves, which will blanket the gravitational wave spectrum below $f \sim 3$ mHz. An example of the expected level of the confusion limit is shown in Figure 1 (Bender & Hils 1997), plotted against the nominal sensitivity curves (Larson 2000) for missions with 5 Gm and 2 Gm armlengths. Strong sources of gravitational waves will rise up above this confusion foreground and be observable by a space-based gravitational wave observatory.

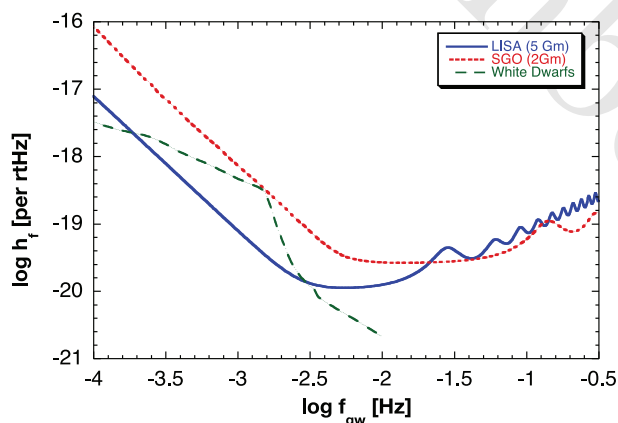


Fig. 1.—: The average gravitational wave power spectral amplitude, h_f , of the confusion foreground due to ultra-compact galactic binaries, plotted against the standard sensitivity curve (Larson 2000) for a 5 Gm (LISA) and 2 Gm (SGO) armlength observatory. The assumed bandwidth is 1 year.

An interesting subset of the ultra-compact binaries are cataclysmic variable stars (CVs), comprised of a primary white dwarf star and a low mass secondary that has filled its Roche lobe and is transferring mass to the primary; several thousand CVs have been cataloged in the Milky Way (e.g., Downes et al. (2001)), but a gravitational

wave detector in space will be sensitive to as many as 20,000 strewn throughout the galaxy. The disparity in number here is the dim electromagnetic brightness of ultra-compact binary systems, which restricts EM detections to those that lie close to Earth, whereas a gravitational wave detector will detect systems of this sort across the entire galaxy. Already, a growing number of ultra-compact binaries and CVs have been observed and characterized with traditional electromagnetic telescopes (Nelemans 2010), a large fraction of which are a class of helium cataclysmic variables (HeCV) similar to the star AM *Canum Venaticorum* (AM CVn). These systems have primary white dwarfs with low mass helium companions providing mass flow onto accretion disks of unknown radii. They are expected to be strong gravitational wave radiators.

Realistic simulations on mock data (Babak et al. 2008, 2010) have shown that tens of thousands of these stars will be detectable by a space-based gravitational wave detector as individually resolved sources (e.g., Crowder & Cornish (2007)), and several hundred of those will be simultaneously detectable by electromagnetic telescopes, even for mission designs more modest in scope than LISA (Littenberg et al. 2013). A population of binaries that can be observed with *both* electromagnetic telescopes and gravitational wave interferometers can be used as probes of the fundamental astrophysics that governs these systems; this multi-messenger mode of observations can reveal information that is difficult or even impossible to extract otherwise.

Models of the accretion disks in HeCV systems have been studied in the past, and suggest the disk radii will be around 75% of the primary Roche radius (Sulkanen et al. 1981a), but this estimate is only certain to within about 10%. Measurements of accretion disk radii in ultra-compact binary systems have been made using eclipsing systems, with results that are accurate to about $\sim 10\%$ (Sulkanen et al. 1981b). Future space interferometry mission concepts (e.g., Peterson (1996); Beichman et al. (1999)) may make direct optical imaging of close binary systems (like AM CVn) possible, allowing a direct measurement of the accretion disk radius. This letter demonstrates how correlating optical observations of a mass transferring CV system with simultaneous gravitational wave observa-

tions by a space-based interferometer can yield a measure of the primary accretion disk's radius.

The paper is organized as follows. Section 2 reviews the conceptual model for the electromagnetic lightcurve and the gravitational wave emission from these systems, as well as the multi-messenger comparison. Section 3 describes our model for overflow and accretion, and our model for the light curve from these systems. Our results and discussion are presented in Sections 4 and 5.

2. Multi-messenger signals

2.1. Electromagnetic lightcurve

Roche lobe overflow through the Lagrange point in ultra-compact binaries will often lead to the formation of an accretion disk around the primary star in mass transferring systems (Lubow & Shu 1975; Paczynski 1977). A model (Warner 1995) that can explain the optical properties of mass-transferring HeCVs has a massive ($\sim 1M_{\odot}$) CO white dwarf embedded in an accretion disk as a primary, and a less massive ($\sim 0.02M_{\odot}$) helium dwarf that has expanded to fill its Roche lobe. Material spills through the inner Lagrange point, streaming onto the accretion disk and causing a bright hot-spot (see Figure 2). This hot spot radiates approximately radially outward from the disk; as the binary orbits, the spot alternately turns towards and away from distant observers, modulating the lightcurve. This model has been applied to AM CVn *in extenso* (Faulkner et al. 1972; Patterson et al. 1992, 1993) and successfully describes a variety of signals present in the photometric lightcurve of this star. Photometric observations have measured an orbital period of $\tau_o = 1028.7325 \pm 0.0004$ s (Harvey et al. 1998), confirming previous theoretical predictions (Patterson et al. 1993).

Electromagnetic observation methods exist for determining accretion disk radii from the lightcurve in *eclipsing* binary systems (Ritter 1980; Sulkkanen et al. 1981a). In eclipsing systems, the accretion disk can be occulted by the secondary, and then can itself occult the secondary a half period later. The contact points of the eclipse in the electromagnetic lightcurve encode the exact position of the binary components, and provide solutions for all the geometric parameters of the binary, including the size of the accretion disk.

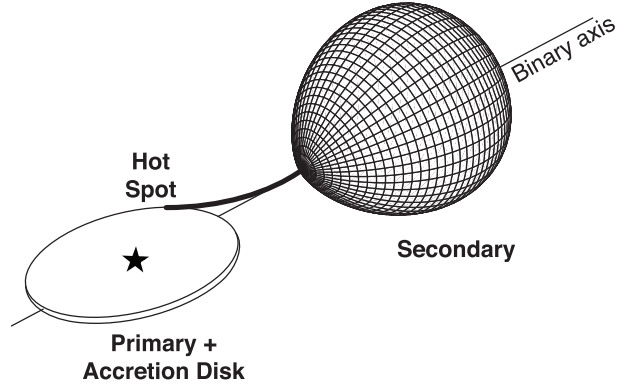


Fig. 2.—: The secondary companion has expanded to fill its Roche lobe, which overflows, forming an accretion disk around the white dwarf primary. The point of accretion impact on the edge of the disk creates a electromagnetically bright hot spot.

The error expected from these eclipsing methods is $\sim 10\%$, estimated by Sulkkanen et al. (1981b).

2.2. The gravitational wave signal

The ultra-compact binaries are strong gravitational wave radiators in the millihertz gravitational wave band. In this regime, with orbital periods on the order of several thousand seconds to tens of seconds, the gravitational wave emission is well described by the quadrupole formula (Peters 1964; Peters & Mathews 1963). The gravitational wave emission extracts energy and angular momentum from the binary on long timescales, until ultimately the components merge (for compact stellar remnants like neutron stars and black holes, the merger occurs at high frequencies, in the regime covered by ground-based gravitational wave detectors like LIGO (Harry & the LIGO Scientific Collaboration 2010)). A particularly useful formulation of the emission from compact binaries utilizing the quadrupole formula is due to (Wahlquist 1987), expressed in terms of standard binary observational parameters (inclination, argument of periapsis, longitude of the ascending node, etc.). The overall strength of the gravitational waves depends on a scaling factor h_o :

$$h_o = \frac{4G^2 m_1 m_2}{c^4 a(1-e^2)D} = \frac{4G^{5/3}}{c^4(1-e^2)} \frac{\mathcal{M}}{D} (2\pi f_o \mathcal{M})^{2/3} \quad (1)$$

where Kepler’s third law has been used to express a in terms of the orbital frequency f_o , D is the luminosity distance, and $\mathcal{M} = (m_1 m_2)^{3/5} / (m_1 + m_2)^{1/5}$ is the “chirp mass” of the system. It is expected that compact interacting binaries will have become circularized through mass transfer and common envelope evolution; gravitational wave emission also tends to circularize binaries. For circular binaries, $e = 0$, and the gravitational wave frequency f is simply related to the orbital frequency by $f = 2f_o$. Then the scaling amplitude is simply

$$h_o = \frac{4G^{5/3}}{c^4} \frac{\mathcal{M}}{D} (\pi f \mathcal{M})^{2/3} . \quad (2)$$

Gravitational wave detectors will detect two polarization states, the strength of which are expressed in terms of the scaling amplitude h_o . Using the quadrupole formula for an arbitrarily oriented circular binary gives (Wahlquist 1987):

$$\begin{aligned} h_+(\theta) &= h_o(\cos(2\phi)A_0 - \sin(2\phi)B_0) \\ h_\times(\theta) &= h_o(\sin(2\phi)A_0 + \cos(2\phi)B_0) . \end{aligned} \quad (3)$$

Here, ϕ can be interpreted as either the binary longitude of the ascending node, or the gravitational wave polarization angle, and

$$A_0 = -\frac{1}{2}[a + \cos^2(\iota)] \cos 2(\theta - \theta_n) \quad (4)$$

$$B_0 = -\cos(\iota) \sin 2(\theta - \theta_n) \quad (5)$$

are orientation dependent functions (additional terms for $e \neq 0$, not treated in this work, may be found in Wahlquist (1987)). The angle θ is the angular position in the orbit (the “true anomaly”), and θ_n is the value of θ at the line of nodes, which we will set to zero for convenience. In a circular binary, the orbital phase angle $\theta(t)$ is related to the gravitational phase angle $\varphi(t)$ by $\varphi(t) = 2\theta(t)$, where $\varphi(t)$ is the phase function of the gravitational wave determined from the orbital dynamics and evolution. The gravitational wave phase for most of the population of ultra-compact binaries is a simple function of the gravitational wave frequency

$$\varphi(t) = ft + \frac{1}{2}\dot{f}t^2 + \phi_0 , \quad (6)$$

where f and ϕ_0 are the gravitational wave frequency and wave phase at $t = 0$, and \dot{f} is the

chirp. The gravitational wave contribution to the chirp, from the quadrupole approximation, is

$$\dot{f} = \frac{96}{5}\pi^{8/3} \frac{G^{5/3}}{c^5} f_0^{11/3} \mathcal{M}^{5/3} . \quad (7)$$

Astrophysical effects (such as spin orbit interactions (Hut 1981), tidal interactions (Willems et al. 2008) or mass transfer (Deloye & Taam 2006)) will alter the angular momentum in the binary, and thus the orbital period and observed frequency f_0 . The ultimate effect is that there are many competing processes that drive the evolution of angular momentum in the system. It is clear that the relative contributions of each physical process will alter the interpretation of the orbital evolution derived from LISA’s gravitational wave observations, a matter that will be considered in a future paper.

A LISA-like detector will have a frequency resolution related to the mission duration T_{obs} given by $\Delta f = 1/T_{obs}$; this is the frequency “bin width” for observations. As T_{obs} lengthens, the bin width narrows. In general, a conservative estimate is that a detector will detect a binary chirping if the frequency evolves by a bin or more during the observing time, or $\dot{f} \gtrsim \Delta f / T_{obs}$. For the known parameters of AM CVn, Eq. 7 predicts an evolution of $\dot{f} = 4.79 \times 10^{-19}$ Hz/s. For a $T_{obs} = 1$ year observation, the limiting chirp would be $\dot{f} = 1$ bin/yr $= 1.00 \times 10^{-15}$ Hz/s; AM CVn’s chirp falls well below this conservative threshold. For the purposes of this work, it is assumed that the binaries are all monochromatic (non-chirping).

A spaceborne interferometer will characterize both polarization amplitudes as part of its deconstruction of the data stream; the ratio of h_+ to h_\times is a direct measure of the inclination angle ι of the binary, as shown in Figure 3. Knowledge of the inclination angle provides further constraints on the model of the electromagnetic lightcurve, making any derived radius of the accretion disk more secure.

2.3. Multi-messenger phase comparison

The multi-messenger comparison being examined in this paper is exploiting the periodic structure in both the gravitational wave and the electromagnetic signals as a probe of the geometry of the source. Consider a circularized ultra-compact binary with orbital frequency f_o . The gravita-

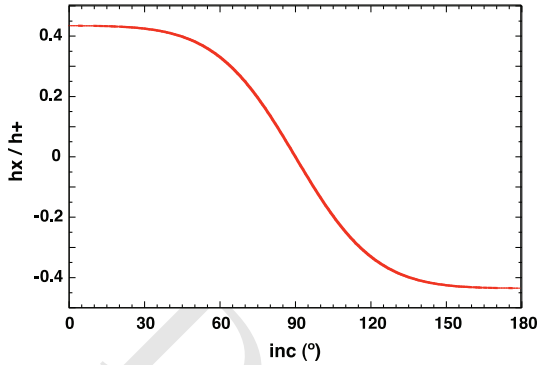


Fig. 3.—: Measuring the ratio of measured gravitational wave polarization amplitudes, h_x/h_+ , is a measure of the binary inclination angle, ι .

tional wave frequency, f , is twice the orbital frequency of the binary, $f = 2f_o$. In this case, the gravitational wave signals peak at the times when the distance between the components of the binary when projected onto the sky plane is minimized, which occurs when one of the components is at its closest distance to the observer. This provides a fundamental marker for the orientation of the binary components in time. By contrast, the electromagnetic lightcurve shows variation (on orbital timescales) corresponding to the underlying components of the binary changing position and orientation with respect to the line of sight. The tool for determining the location of those structures, by measuring them against the reference provided by the gravitational waves, is the measured phase difference between the arriving gravitational waves and the electromagnetic lightcurve.

The phase difference between the lightcurve and the gravitational waves at any observation time t is

$$\Phi(t) = \phi_{gw}(t) - \phi_{em}(t) = 2\pi t(f_{gw} - f_{em}) + \alpha, \quad (8)$$

where α is a phase offset between the gravitational waves as compared to the electromagnetic lightcurve at the time of measurement. The term α can encode a variety of physical and geometric effects, but in principle can be divided into two basic flavors: effects that delay propagation after the signals are emitted, and model dependent delays that produce phase offsets when the signals are originally generated in the system.

For propagation delays, there are two funda-

mental origins. First, gravitational waves and photons could propagate at intrinsically different speeds. General relativity predicts that gravitational waves should propagate at $v_{gw} = v_{em} = c$, but as a matter of observational science this can be tested using multi-messenger observations like those described here (Hazboun & Larson 2013). As the expectations are for general relativity's predictions to be correct, this paper assumes gravitational waves will propagate at the speed of light: $v_{gw} = c$. A second fundamental delay during propagation could be experienced by the photons, traveling through media with non-unit index of refraction: first through the interstellar medium, and then through the Earth's atmosphere. Given the typical distance to sources that will be simultaneously detectable in both EM and GW spectra, the typical phase delay from propagation delays is estimated to be $\alpha_{prop} \sim 5 \times 10^{-11}$, about 4 orders of magnitude less than the expected accuracy of the raw phase measurements themselves (Larson & Hiscock 2000), and can be safely neglected for this analysis.

For geometric and model dependent phase differences, one must consider the structure of the waves being observed. The gravitational wave structure is simple. The ultra-compact binaries being considered here are assumed to be circular and monochromatic, with the waveforms being accurately described by the quadrupole radiation formula. In this context, the gravitational waves are sinusoidal. Even for systems that harbor small amounts of eccentricity, the signals will still be exceedingly clean (both cases are shown in Figure 4). The peaks in the gravitational wave signals correspond to times when the binary components reach their closest distance to the observer; thus, the gravitational waves provide an absolute reference for locating the binary axis orientation as a function of time. There is an ambiguity associated with the quadrupolar nature of the gravitational radiation pattern — it peaks when one component is at its closest distance to the observer, but also 180° away in the orbit, when the positions of the binary components are reversed (this is most obviously indicated in the gravitational wave frequency, which is twice the orbital frequency, $\omega_g = 2\omega_{orb}$).

By contrast, the electromagnetic lightcurve is rich in structure, with shapes and peaks in the

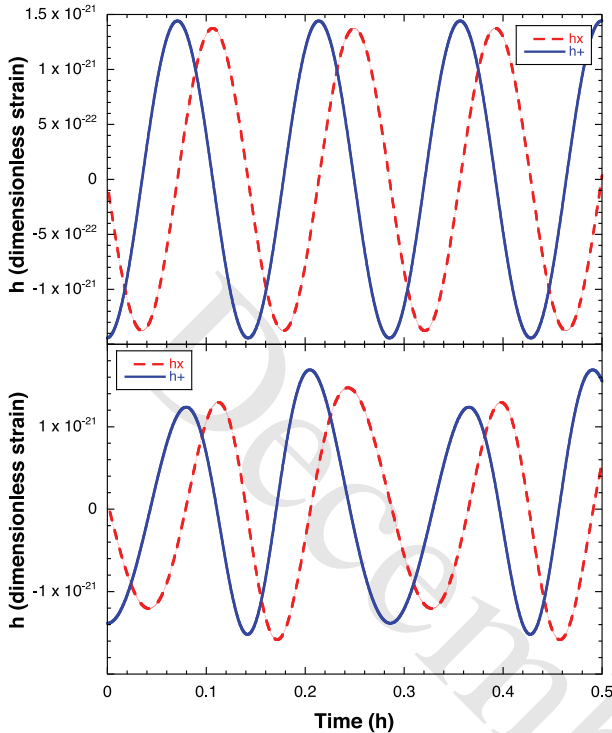


Fig. 4.—: Simulated gravitational wave signals for AM CVn using current, best known parameters Nelemans (2010). Top panel shows the signal for a purely circular, monochromatic system. Lower panel illustrates how signal changes if system had moderate eccentricity ($e = 0.1$), but otherwise identical parameters.

curve being the result of the changing aspect of the system’s internal components during the course of an orbit. There are several primary contributions to the lightcurve shape: emission from the white dwarf primary; emission from the Roche expanded secondary giving ellipsoidal variations as the secondary shape rotates relative to the line of sight; emission from the accretion disk; and lastly, emission from the hot spot where the overflow stream impacts the accretion disk. Consequently one must choose where we want the gravitational wave signal and the lightcurve signal to line up, and the offset from this alignment point to the point of zero binary phase constitutes the geometrical part of α .

In this paper we are interested in characterizing the accretion disk radius by measuring the phase of the hot spot compared to the phase of

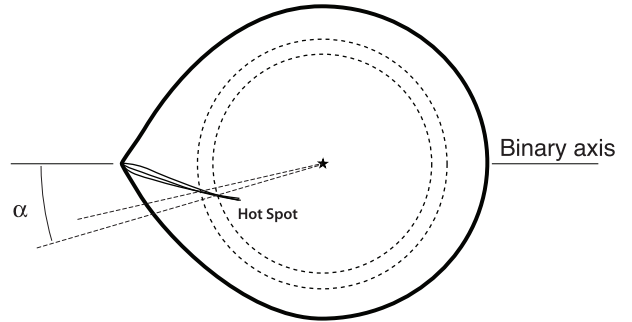


Fig. 5.—: The overflow stream from the donor creates a hot spot at the impact point on the accretion disk. The value of the angle α_* depends on the radius of the accretion disk.

the gravitational wave signal. In this context then, the value of the parameter α in Eq. 8 is affected by the geometric angle α_* illustrated in Figure 5, the angle between the binary axis and the impact point on the accretion disk. For a given model of the overflow stream, the measured value of α_* will correspond to a unique accretion disk radius. The ability to measure α_* will be limited by the errors associated with each of the independent phase measurements, and by our ability to recognize the contribution of the hot spot to the electromagnetic lightcurve.

3. A simple model for ultra-compact mass overflow binaries

3.1. Model System: AM CVn

Many ultra-compact binaries have already been identified as candidate *verification binaries* for space-based gravitational wave detectors (Nelemans 2010). For the purposes of demonstration, this paper uses as canonical parameters the current known values for *AM Canum Venaticorum* (AM CVn), the archetype for a large number of ultra-compact binaries that are expected to be visible in gravitational waves. The physical parameters for AM CVn are: $m_1 = 0.68M_\odot$, $m_2 = 0.125M_\odot$, and $\omega = 6.108 \times 10^{-3} \text{ s}^{-1}$ (a circular binary with semi-major axis $0.21R_\odot$). The disc radius is estimated to be $R_d = 0.478a$ (Solheim et al. 1998) The temperature parameters were estimated by minimizing the L_2 error between the output of our lightcurve model (see section 3.3) and the observed lightcurve. A temperature $T = 10^4 K$ is

Table 1:: AM CVn Simulation Parameters

Parameter	Notation	Value	Reference
Mass 1	m_1	$0.68M_\odot$	1
Mass 2	m_2	$0.125M_\odot$	1
Orbital Period	P_{orb}	1028.73 s	2
Inclination	ι	43°	1
Luminosity Distance	d	606 pc	1
Disc Radius	R_{disc}	$0.48a$	3
Char. Disc Temp.	T_{disc}	90000 K	Fit
Pole Temp.	T_{pole}	15065 K	Fit, 4
WD Temp.	T_{WD}	19473 K	Fit
Max HS Temp.	T_{HS}	131000 K	Fit
HS Cooling Parameter	ζ	2.9828	Fit

Notes. Parameters below the horizontal line are fitted using our lightcurve model.

References. (1) Roelofs et al. 2006; (2) Harvey et al. 1998;

(3) Solheim et al. 1998; (4) Roelofs et al. 2006.

adopted as an initial guess for the pole temperature of the secondary (Roelofs et al. 2006).

3.2. Overflow simulations

3.2.1. Equations of Motion

In order to demonstrate this method for measuring the accretion disk radius, a simple model of the accretion overflow was created using the restricted three body approximation (Flannery 1975). In the co-rotating frame of the binary, the accelerations on a fluid particle in the x and y directions may be written as

$$\ddot{x} = -\frac{Gm_1}{r_1^3} \left(x - \frac{aq}{1+q} \right) - \frac{Gm_2}{r_2^3} \left(x + \frac{a}{1+q} \right) + \omega^2 x + 2\omega\dot{y} - \xi\dot{x}, \quad (9)$$

and

$$\ddot{y} = -\frac{Gm_1}{r_1^3} y - \frac{Gm_2}{r_2^3} y + \omega^2 y - 2\omega\dot{x} - \xi\dot{y}, \quad (10)$$

Here $\omega = 2\pi f_{orb}$ is the orbital angular velocity of the stellar components, $q = m_2/m_1$ is the mass ratio, and ξ is a parameter that characterizes the viscous drag on the fluid element.

In simulation, the equation is non-dimensionalized by introducing scaling factors M (total mass) for mass, a (binary separation) for length, ω^{-1} for time, and GM/a for potential. The dimensionless

equations then read

$$\begin{aligned} \tilde{x}'' &= -\frac{\mu}{\tilde{r}_1^3}(\tilde{x} - \tilde{a}Q) - \frac{(1-\mu)}{\tilde{r}_2^3} \left(\tilde{x} + \frac{\tilde{a}}{q}Q \right) \\ &\quad + \tilde{x} + 2\tilde{y}' - \tilde{\xi}\tilde{x}' \\ \tilde{y}'' &= -\frac{\mu}{\tilde{r}_1^3}\tilde{y} - \frac{(1-\mu)}{\tilde{r}_2^3}\tilde{y} + \tilde{y} - 2\tilde{x}' - \tilde{\xi}\tilde{y}', \end{aligned} \quad (11)$$

where \tilde{x} and \tilde{y} are dimensionless coordinates, $\tilde{\xi}$ is the dimensionless viscosity coefficient, μ is the mass fraction $\mu = m_1/M$, $Q = q/(1+q)$, and prime denotes differentiation with respect to the dimensionless time variable.

These equations are simultaneously numerically integrated to give the position and velocity of particles in the overflowing accretion stream. The geometric information regarding the position of the stream is an essential player in the determination of the accretion disk radius, and the stream particle velocity at disk impact is used in the energetic calculations that give the model brightness for the hot spot.

From this point on, tildes will be dropped and quantities discussed in the context of the overflow simulation will be the dimensionless variables.

3.2.2. Stream Coherence

Early numerical simulations (Flannery 1975) of matter overflow in cataclysmic variables suggested the stream maintains coherence as it falls toward impact. Coherence in the overflow stream through

impact with the primary accretion disk is a necessity to understanding the variable lightcurve created by cataclysmic variable stars such as AM CVn. To evaluate the stream coherence in this model, initial velocity data for Eq. 11 were drawn from the Maxwell-Boltzmann Speed Distribution:

$$f(v) = \frac{\sqrt{\frac{2}{\pi}} v^2 \exp(\frac{-v^2}{2\eta^2})}{\eta^3} \quad (12)$$

where η is determined by the thermal coefficient:

$$\eta = \sqrt{\frac{kT}{m}} \quad (13)$$

and k , T and m are Boltzmann's constant, the temperature of the secondary, and the mass of the particle in the stream. The velocities were constrained by angle $\theta = \pm 57^\circ$, the maximum opening angle of the gravitational equipotential that passes through the inner Lagrange point.

Taking the canonical particle mass to be the mass of a proton, the simulation was run 2,500 times pulling randomly from the speed distribution and attaching that speed to an angle drawn from a uniform distribution in the range of θ . Results of this simulation are shown in Figure 6, in the co-rotating frame of the binary. This histogram show the injected parameters, while the trajectory plot shows overlays of all 2,500 runs in the equipotential space dominated by the white dwarf (the vertex of the equipotential boundary drawn at $y = 0$ is the Lagrange point between the primary and secondary). All of the trajectories, irrespective of initial conditions at the overflow point, coalesce around a central trajectory.

3.2.3. Hot Spot Phase Angle

Based on the stream coherence simulation, the trajectory of the matter overflow stream is known until the time it intersects the accretion disk. The HS phase offset angle, α_* , is measured from the binary axis (located from the gravitational waves) to the hot spot impact point (measured from the electromagnetic lightcurve), and using the trajectory model yields the accretion disk radius at which the trajectory crosses the angle α_* (*i.e.*, the radius of the disk when it intersects the matter stream). For the AM CVn demonstration parameters, Figure 7 displays calculated values of the HS phase offset

angle α_* for a range of disc radii lying within the primary's Roche radius. Larger disc radii show a small spread in impact angles ($\sim 2^\circ$), a consequence of tight stream coherency, while smaller radii result in a larger impact spread (as high as $\sim 10^\circ$) due to the oblique angle of attack at impact.

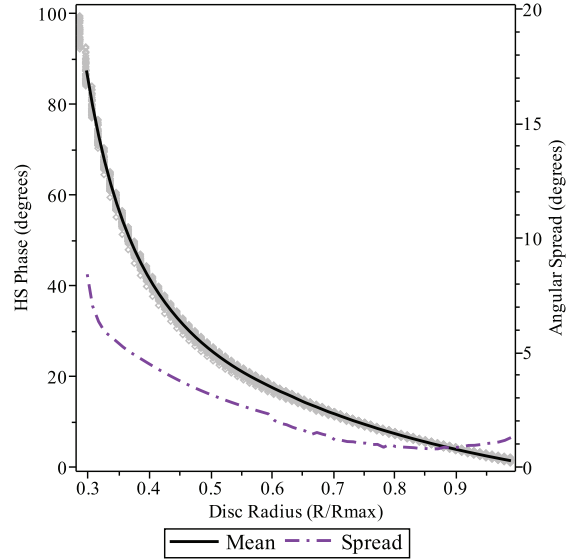
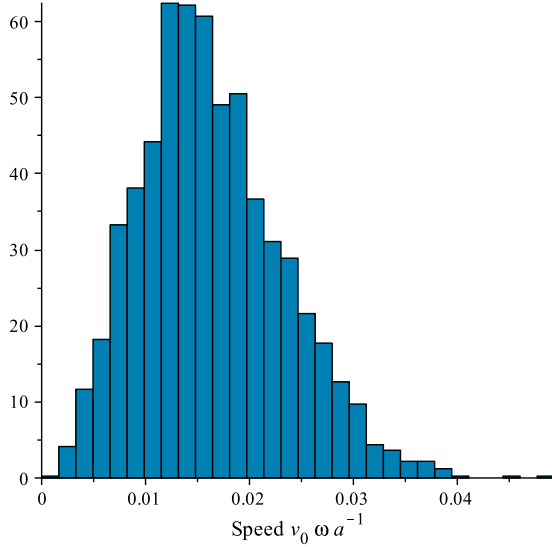


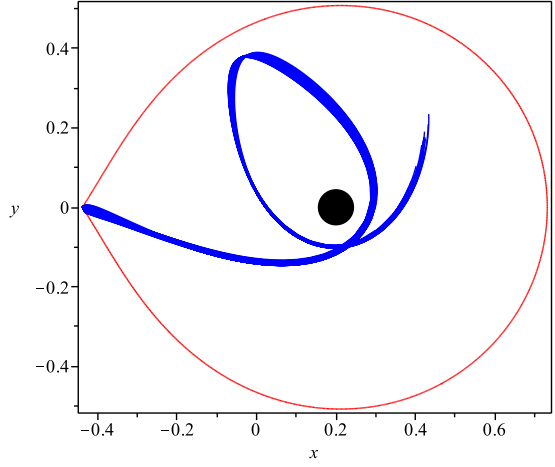
Fig. 7.—: Stream impact angle α_* for various disc radii, ranging up to the size of the primary Roche Lobe. Radius values are scaled by the value R_{max} , which is defined as the distance from the primary to the $L1$ Lagrange point. The grey envelope shows the spread of impact angles for a random selection of initial velocities, while the black line plots the mean of the spread. The dashed line plots the angular spread of the stream impact with values on the right vertical axis.

3.2.4. Viscosity Term

The overflow stream consists of a collection of infalling particles, which will have some measure of interaction with each other, plausibly influencing the trajectory. To explore this, a dimensionless viscosity parameter is used in the equations of motion, Eq. 11. In general, this value is expected to be small, $\xi \lesssim 0.1$, but even smaller values are typical in modern accretion simulations (Kley et al. 2008), to the point of using inviscid flow (Sawada & Matsuda 1992). By examining the range of ξ



(a) Histogram of sampled speeds with most probable speed $v_p = \sqrt{2}\eta = 0.0145$.



(b) Overflow stream simulation for AM CVn parameters. Stream is visually observed to maintain coherency until self-impact.

Fig. 6.—: Overflow stream simulation figures.

over which the stream crosses itself, it is seen that neither the mean impact angle nor the angular spread vary significantly in the range $0 \leq \xi \leq 0.3$ (see Figure 8). For viscosity values larger than $\xi \gtrsim 0.3$, these simulations enter the regime where the stream will not cross itself, but rather it will impact the primary directly, resulting in no disc formation. This implies that the stream viscosity does not significantly affect the angle α_* . A value of $\xi = 0.06$ is adopted for the simulations presented here.

3.3. Lightcurve simulations

Since simultaneous, coordinated electromagnetic and gravitational wave observations of ultra-compact binaries do not exist (yet), simulated lightcurve data are generated for this study. Lightcurves are generated via a simple geometric model with numerically modeled accretion implemented in a MATLAB program. In this simulation, a close binary system with an accretion disc and a hot spot is rotated in three dimensions, and the observed portions of the bodies in the system are used to generate a synthetic lightcurve. This is a geometry based simulation; physical processes such as gravitational attraction are not explic-

itly computed. This is a well known basis for lightcurve simulations, e.g. Wilson & Devinney (1971).

3.3.1. Setup

There are four distinct objects in the simulation: the primary star, the accretion disc, the hot spot, and the Roche lobe filled by the secondary star. Three dimensional point clouds are generated for each object in appropriate orbital positions, which are then used to compute the three dimensional *convex hull* of each object. The convex hull of a 3-D point cloud is a triangulation of the bounding surface of the cloud, i.e. a set of vertex-connected triangles such that all points in the cloud are either triangle vertices or interior to the surface formed by the triangulation. For each triangle in the triangulation, the geometric center, area, and normal vector are computed. Temperature profiles (described in the next section) are mapped onto the objects by assigning a temperature for each triangle in the convex hulls, based on input parameters for the simulation. The simulation can be run for as long as desired to generate lightcurves of arbitrary length.

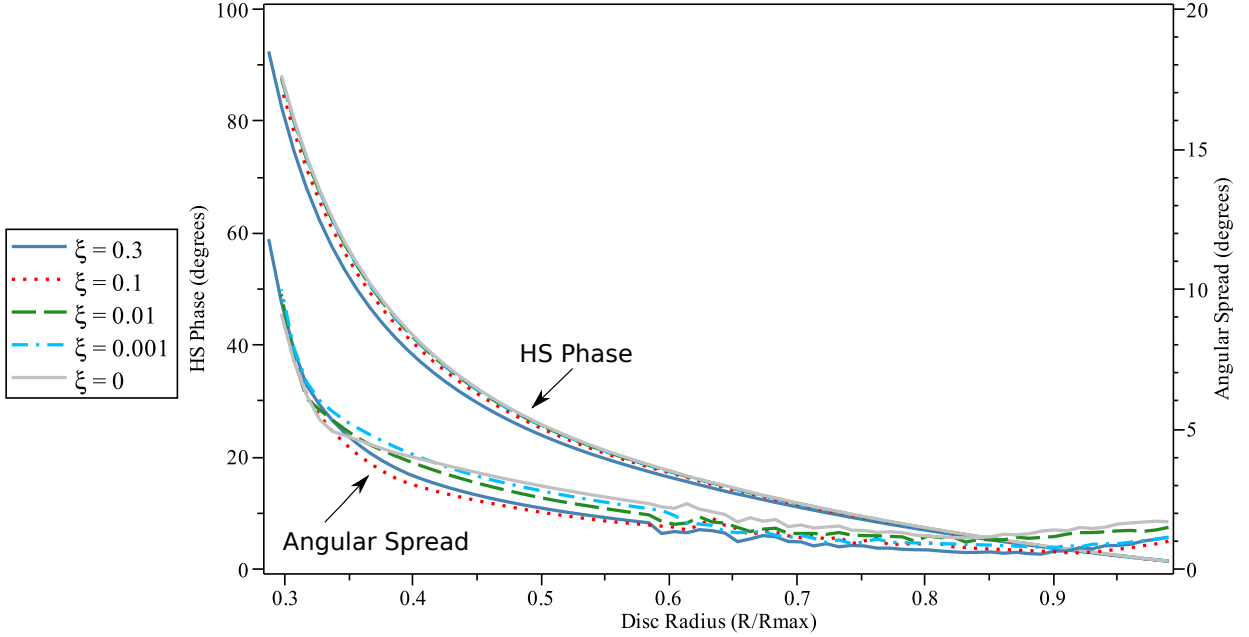


Fig. 8.—: HS phase offset angle α_* for various values of dimensionless viscosity ξ . Note that the mean impact angle and angular spread are essentially unchanged over many orders of magnitude.

3.3.2. Temperature Profiles

Temperature values for the Roche Lobe are generated by the law of gravity darkening, $T_e \propto g^{1/4}$ (Lucy 1967; von Zeipel 1924). This leads directly to an expression for the temperature at any point on the Roche Lobe given the pole temperature T_{pole} :

$$\frac{T(x, y, z)}{T_{\text{pole}}} = \left[\frac{g(x, y, z)}{g_{\text{pole}}} \right]^{1/4} \quad (14)$$

where T_{pole} and g_{pole} are the values of temperature and gravitational acceleration at the star pole. T_{pole} is generally taken to be the effective temperature of a comparable field star (Orosz & Bailyn 1997), and g_{pole} can be found by taking the gradient of the known gravitational potential at the pole of the Roche Lobe.

The temperature profile for the disc is a simple energy conservation based model given by

$$T = T_{\text{disc}} \left(\frac{R}{r} \right)^{3/4} \left(1 - \sqrt{R/r} \right)^{1/4} \quad (15)$$

where

$$T_{\text{disc}} = \left(\frac{3Gm_1\dot{m}_1}{8\pi\sigma R^3} \right)^{1/4} \quad (16)$$

is a characteristic temperature of the disc with \dot{m}_1 the mass transfer rate, R the radius of the primary, r the radial distance out from the center of the disc, and σ the Stephan-Boltzmann constant.

The hot spot is modeled as a sphere with center located at the edge of the accretion disc, and assigned an exponentially decaying temperature profile according to

$$T(\hat{x}) = (T_{\text{HS}} - T_d) \exp(-\zeta\hat{x}) + T_d \quad (17)$$

where \hat{x} is a dimensionless coordinate that ranges from $0 \leq \hat{x} \leq 2$, given by $\hat{x} = (s - s_{\text{CM}})/R_{\text{HS}} + 1$, s is the radial distance of the center of the hot spot from the primary, s_{CM} is the center of the hot spot, R_{HS} is the radius of the hot spot, T_{HS} is the maximum temperature on the hot spot, T_d is the outer disc temperature, and ζ is the spatial cooling rate.

The primary white dwarf temperature is set as a constant value over a sphere.

3.3.3. Geometric Flux Projection

The lightcurve simulation assumes that the observer is positioned far away on the negative z -axis, in which case the xy -plane is the sky plane

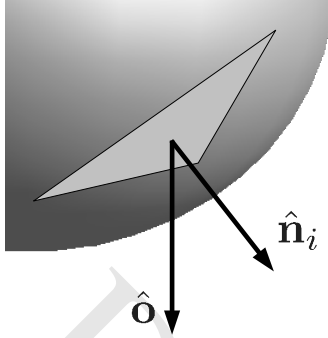


Fig. 9.—: Illustration of observer vector and triangle normal vector, overlaid on a convex hull element at the stellar surface.

for the observer. At each time step, a point on the synthetic light curve is computed as follows. For the four objects in the simulation, the normal vectors for each triangle in the convex hull triangulations are examined to determine if the value of the z component is negative, i.e. has a component pointing toward the observer. Triangles failing this condition are discarded for this iteration. Next, the objects are ordered based on their z coordinate, essentially from lowest to highest. The triangle centers of the first object in the order are projected onto the xy -plane. Subsequent objects are also projected, however care is taken to avoid overlap of the objects by use of a 2-D convex hull and a standard point-in-polygon algorithm. Triangles whose projected centers lie interior to the convex hull of a previously projected object are discarded, thus ignoring those triangles occulted by other objects in the system.

The luminosity of each triangle visible to the observer is calculated using the Stefan-Boltzmann law. Total flux arriving at Earth is then computed using the standard flux-luminosity relationship, summed over $\mathcal{V}(t_k)$, the set of all visible triangles at the k th time step:

$$F(t_k) = \sum_{i \in \mathcal{V}(t_k)} \frac{\sigma A_i T_i^4 (\hat{\mathbf{o}} \cdot \hat{\mathbf{n}}_i)}{4\pi D_E^2} \quad (18)$$

where A_i and T_i are the area and temperature of the i th triangle, respectively, $\hat{\mathbf{o}}$ is the unit vector pointing toward the observer, $\hat{\mathbf{n}}_i$ is the unit vector normal to the i th triangle (see Figure 9), and D_E

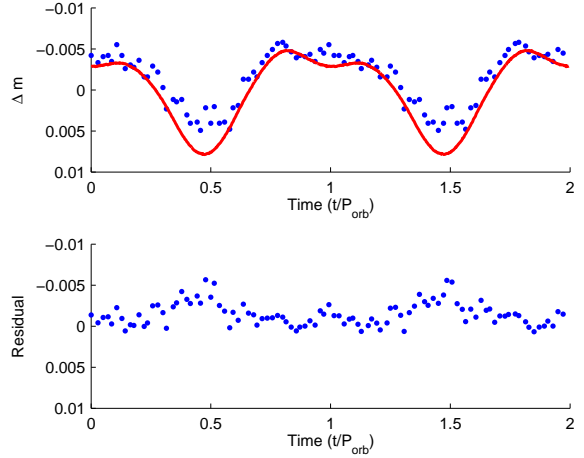


Fig. 10.—: Simulated lightcurve for AM Canum Venaticorum in the top panel, displayed as magnitude deviation from mean, Δm . Solid line shows simulation output, dots represent actual AM CVn data (Harvey et al. 1998). Bottom panel shows residuals between model and observation.

is the distance to Earth.

This simulation calculates only raw bolometric blackbody luminosities; more detailed effects such as frequency specific flux, reflectance, etc. are not included. For the purpose of this paper, however, these omissions are acceptable. A lightcurve generated for the AM CVn model parameters is plotted against observed lightcurve data in Figure 10.

3.4. GW Phase Calibration

[eric: Expand this explanation to stress how important this is. This is the key for the multi-messenger aspect of the method.]

The $h_+(t)$ and $h_\times(t)$ waveforms in Eq. 3 represent the expected signals that will be observable by a gravitational wave observatory. These expressions can be solved for θ to give an estimate of the binary phase as a function of time:

$$\hat{\theta}(t) = \frac{1}{2} \cos^{-1} \left(\frac{2\sqrt{\tilde{h}_+^2(t) + \tilde{h}_\times^2(t) - \cos^2(\iota)}}{\sin^2(\iota)} \right) \quad (19)$$

where \tilde{h}_+ and \tilde{h}_\times are the measured waveform amplitudes scaled by h_o , e.g. $h_+ = h_o \tilde{h}_+$.

There is a four-fold degeneracy in Eq. 19 due to the square root and inverse cosine. This results

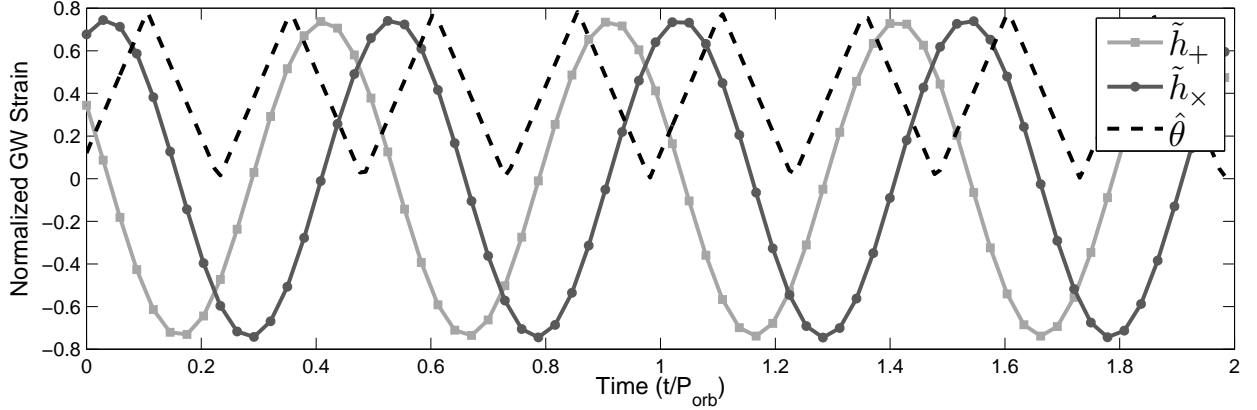


Fig. 11.—: Gravitational wave signals \tilde{h}_+ and \tilde{h}_\times , as well as the estimated phase value $\hat{\theta}$. Note that there are four locations where $\hat{\theta} = 0$ in each orbital period, indicating the quadrature and conjunction phases. [eric: Updated the language in this caption a bit, and redid the figure for better label size]

in four locations where $\hat{\theta} = 0$ during each binary orbit, corresponding to the phases where the projected distances between the binary components are maximized or minimized i.e. the quadrature and conjunction phases. The model lightcurve uses a value of $\phi = 25^\circ$, resulting in gravitational wave signals and phase estimate as shown in Figure 11.

4. Model Implementation and Demonstration

Our accretion disc radius estimation method is now described explicitly and applied to the AM CVn system. Lightcurve data from our model and the actual observed lightcurve Harvey et al. (1998) are both used to demonstrate the method. Gravitational waveforms and model lightcurves are generated using the model parameters in Section 3.1. Since gravitational wave observations do not yet exist for this system, we regard this as a test of the method with partially real data.

We assume that fundamental parameters of the system can be extracted, i.e. component masses, secondary temperature, orbital period, inclination, and luminosity distance, from which a stream overflow model and lightcurve model for the ellipsoidal variations (EV) can be generated. We also assume that the gravitational wave signals $h_+(t)$ and $h_\times(t)$ have been disentangled and are separately available. There will be a substantive number of multi-messenger binaries that can be si-

multaneously observed in EM and GW spectrums (Littenberg et al. 2013); the gravitational wave data will provide accurate values for the component masses, the orbital period, and the inclination, all of which will inform the modeling described here. [eric: This paragraph may be the right place to add in a note about the uncertainty in parameters, notably the individual component masses. We should also acknowledge that while we are using ideal GW waveforms (which I noted that we assume are separated by polarization), there will be some amount of noise with real observations. Just make a note of it and move on.]

The method proceeds as follows:

- Model accretion stream
- Model ellipsoidal variations
- Use GW signal to calibrate lightcurve to orbital phase
- Subtract EV from observational data – remaining modulation should be due to hot-spot
- Determine phase offset between binary axis and hot-spot
- Use stream overflow model to determine radius of disc

4.1. System Modeling

The methods outlined in Section 3.3.3 have been used to model the AM CVn lightcurve, which is shown against the observed lightcurve in Figure 10. Using our model parameters, the calculated magnitude for this simulation is $m_{\text{sim}} \approx 14.18$, which matches the accepted value for AM CVn.

The model output shown in figure 10 displays the residuals between the observed data and the model fit in the bottom panel. The model performs reasonably well in recreating the qualitative features of the observed data given its simplicity, though it greatly overestimates the amount of dimming that occurs during the quadrature phases. These errors are likely due to omitting physical effects such as reflectance and limb darkening that would have small but noticeable effects on the total flux output.

Our lightcurve model is used in two ways. First we assume that the model lightcurve generated by simulating the full AM CVn system is the observed lightcurve and proceed with the method from there, showing that the method can recover the disc radius well for the simulated data. In parallel we work with the *true* lightcurve data where the full system model is not used. For each case a model of the EVs are required to perform the subtraction which results in the hot spot modulation, and so each demonstration utilizes the EV model generated by our simulation. Given the simple and predictable nature of EVs, this is a reasonable course of action.

4.2. EV Subtraction

In order to locate the hot spot phase, the contribution to the lightcurve from the EV must be modeled and removed. The resulting EV from our model using the AM CVn parameters from table 1 is shown in Figure 12.

In section 3.4 the method for identifying the quadrature and conjunction phases using the gravitational wave signals was described. To compute the hot spot phase offset from the binary axis, we need to identify the conjunction phase in which the secondary Roche lobe is closest to the observer, as the hot spot flux should peak briefly before that time. It is the phase difference between the hot spot flux peak and the following conjunction phase that we interpret as the hot spot phase offset. Us-

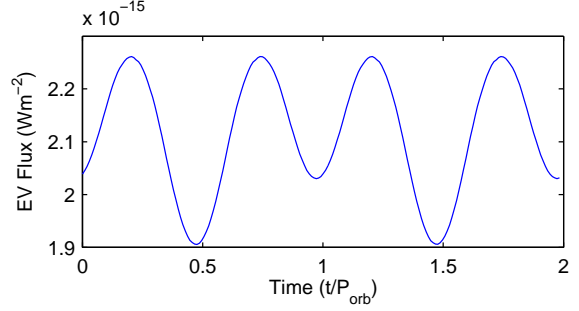


Fig. 12.—: Ellipsoidal variation model output for Am CVn. This curve will be subtracted from observed lightcurve to find the HS modulation after the correct initial phase θ_0 is found.

ing the synthetic GW signals, a binary phase estimate $\hat{\theta}(\tilde{t})$ is generated and shown in figure 11. The conjunction and quadrature phases are identified as the points where $\hat{\theta}(\tilde{t}) = 0$ ($\tilde{t} \equiv t/P_{\text{orb}}$), and since our EV model treats a quadrature phase for $\theta = 0$, the initial phase θ_0 for the EV model will take one of four values

$$\theta_{0,i} = 2\pi(1 - 0.25i - \tilde{t}_0) \quad (20)$$

where $i \in \{0, 1, 2, 3\}$, and \tilde{t}_0 is the first location where $\theta(\tilde{t}) = 0$.

Based on the overflow trajectory simulations, we expect the phase of the HS peak output to lead the appropriate conjunction phase. We make the reasonable assumption that the peak in the lightcurve corresponds closely to the peak in received hot spot flux, and so we choose the valley in $\hat{\theta}$ just behind the lightcurve peak to be the appropriate conjunction phase, making the previous $\tilde{t} = 0$ point the quadrature phase we want for the initial EV phase, i.e. the point near $\tilde{t} = 0.75$ in our demonstration data.

With both the EV model and initial phase estimate in hand, the estimated hot spot modulation can be found by performing the subtraction $HS = OD - EV$ (abbreviations from table 2). If the correct initial phase was chosen, the remaining variation in the lightcurve should be due to either HS modulation or eclipses. The subtraction results are shown in figure 13 for both the full model simulation (solid red curve) and the actual observed data (blue dots). The top panel illustrates the result of choosing an incorrect \tilde{t}_0 as the

initial phase for the EV model, while the bottom panel shows the result of choosing the correct initial phase as described previously.

Table 2:: Lightcurve Abbreviations

Abbreviation	Meaning
OD	Observed lightcurve data
HS	Hot spot modulation
EV	Ellipsoidal variations

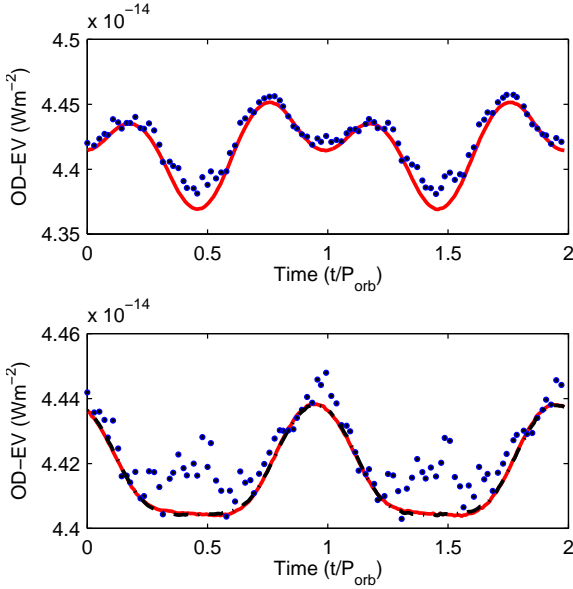


Fig. 13.—: Results of the $HS = OD - EV$ subtraction for both the model data (red line) and observed data (blue dots) using the conjunction phase (incorrect) as θ_0 (top panel) and the quadrature phase (correct) as θ_0 (bottom panel). Also plotted in the bottom panel is the actual HS output from the model (black dot-dash). The model subtraction result matches very closely to the model HS output, but not perfectly due to errors discussed in the text.

4.3. Disc Radius Estimate and Errors

The subtraction $HS = OD - EV$ yields what should be the modulation in the lightcurve due to the hot spot flux. From here it is possible to estimate the phase at which the hot spot flux peaks (the face-on view), and therefore compute a value for the HS phase angle α_* .

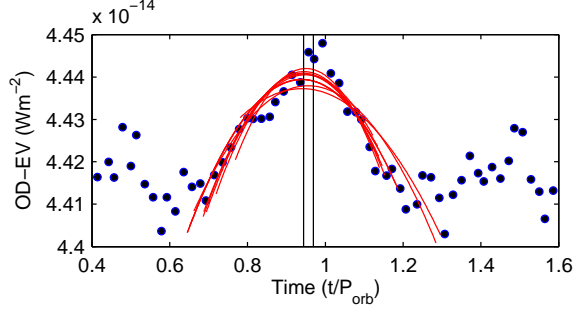


Fig. 14.—: The parabola fitting procedure used to estimate the location of the observed HS peak output. Parabolas are fit to random subsets of the data surrounding the apparent peak near $t = 1$. The average peak location (left hand black line) is found and regarded as the true peak location, θ_{HS} , which is then used to find the HS phase offset, ϕ_{HS} , relative to the subsequent conjunction phase (right hand black line).

Noise exists in both the simulated data and the observed data. In the simulated data this arises from the fact that the simulation samples are taken at a realistic rate (60 Hz), and numerical noise that is introduced by the finite discretization of the body surfaces. Due to the noise present in the lightcurves, we estimate the location of maximum HS flux output by fitting parabolas to random subsets of the lightcurve data surrounding the apparent peak in the $HS = OD - EV$ subtraction and taking the mean of the resulting parabola vertex locations as the orbital phase of the HS peak flux output θ_{HS} . This process is illustrated in Figure 14. The HS phase offset ϕ_{HS} is then estimated by finding the phase difference between θ_{HS} and the conjunction phase following the initial phase, i.e. $\phi_{HS} = (\theta_0 + \pi/2) - \theta_{HS}$, and the corresponding disc radius is identified from the accretion stream simulations described in Section 3.2.

For the model data using the random parabola procedure, we find a HS phase offset of $\phi_{HS} = 7.76^\circ \pm 1.6^\circ$. Using the overflow stream simulation, we find a corresponding disc radius estimate of $\hat{R}_D/a \approx 0.476 \pm 0.025$, where the error bars arise from various parabola fits. This gives an error for the mean value of $\approx 0.4\%$ when compared with the accepted value of 0.478a.

The noisy nature of the true observed data

makes it less clear where the HS peak flux lies. We attempt the same fitting procedure and find HS phases in the approximate range $\phi_{HS} = 7.6^\circ \pm 2.8^\circ$. This translates to an estimated disc radius of $\hat{R}_D/a \approx 0.481 \pm 0.05$. With this method we find an estimation error of $\approx 0.6\%$.

5. Discussion

The method described here is an independent method that is applicable to mass-transferring galactic binaries observable by multi-messenger campaigns involving gravitational wave and electromagnetic observatories. It is a method for measuring the accretion disk radius in any compact binary system, *whether it is eclipsing or not*.

Recent work has estimated that with even modest, sub-meter class telescopes, there will be hundreds of ultra-compact binaries that will be simultaneously detectable in gravitational waves and with EM telescopes (Littenberg et al. 2013); thousands will be observable with multi-meter class telescopes, opening the potential to characterize the physical nature of an entire population of mass transferring binaries.

The model described here for measuring accretion disk radii assumes the primary variation in the optical lightcurve can be identified with a radiating hot spot on the disk, rotating about the primary with the orbital frequency, ω_o . In low mass ratio systems like AM CVn, it has been predicted that the accretion disk will suffer tidal instabilities, deforming it into an eccentric precessing disk, resulting in the phase offset angle varying in time, $\alpha_\star = \alpha_\star(t)$. This instability was first recognized in SU UMa stars, and is thought to be responsible for the “superhump” phenomena in the optical signature of CV stars. The lightcurve of AM CVn is known to exhibit a superhump signature, which could complicate the measurement of the optical phase if it were not well characterized, especially when tracked over long time periods.

The superhump mechanism has been well studied, and there is a known relationship between the periods of the binary orbit (τ_o), the precessional period of the accretion disk (τ_{aa} , period of apsidal advance), and the superhump signature (τ_{sh}) given by

$$\tau_o^{-1} = \tau_{sh}^{-1} + \tau_{aa}^{-1}. \quad (21)$$

For AM CVn, all three periods have been mea-

sured ($\tau_o = 1028.77$ s, $\tau_{sh} = 1051.2$ s, and $\tau_{aa} = 13.38$ hr; (Patterson et al. 1993), (Harvey et al. 1998)). This allows the lightcurve to be reduced and a measurement of the accretion disk made using the difference in phase with a gravitational wave signal. In principle, the presence of the superhump signature, together with the disk radius measurements described here, could be used in concert with gravitational wave observations to measure the ellipticity of the accretion disk. This in turn can provide a method to probe theoretical models of the pressure profile of the accretion disk (Goodchild & Ogilvie 2006). This will be the focus of a future paper.

The analysis presented here also depends crucially on knowledge of the trajectory of the matter stream which overflows from the secondary Roche lobe into the sphere of influence of the white dwarf. If the hydrodynamic simulations of the overflow present an accurate picture of the trajectory, then gravitational wave observations can provide a new tool for probing the physical character of astrophysical systems.

The author wishes to thank M. B. Larson for helpful discussions and suggestions during the course of this work, and the late W. A. Hiscock for first suggesting the possibility of comparing phase measurements to probe ultra-compact binaries. This work was supported by NASA award NNX13AM10G.

REFERENCES

- Amaro-Seoane, P., Aoudia, S., Babak, S., et al. 2013a, GW Notes, Vol. 6, p. 4-110, 6, 4
- . 2013b, NASA RFI Stuy, 6, 4
- Babak, S., Baker, J. G., Benacquista, M. J., et al. 2008, Classical and Quantum Gravity, 25, 184026
- . 2010, Classical and Quantum Gravity, 27, 084009
- Beichman, C. A., Woolf, N. J., & Lindensmith, C. A. 1999, The Terrestrial Planet Finder (TPF) : a NASA Origins Program to search for habitable planets
- Belczynski, K., Kalogera, V., Rasio, F. A., et al. 2008, ApJS, 174, 223

- Bender, P. L., & Hils, D. 1997, *Classical and Quantum Gravity*, 14, 1439
- Bender, P. t. 1998, LISA Pre-Phase A Report, Tech. rep., Max-Planck-Institut für Quantenoptik, Garching
- Crowder, J., & Cornish, N. J. 2007, *Phys. Rev. D*, 75, 043008
- Deloye, C. J., & Taam, R. E. 2006, *ApJ*, 649, L99
- Downes, R. A., Webbink, R. F., Shara, M. M., et al. 2001, *PASP*, 113, 764
- Faulkner, J., Flannery, B. P., & Warner, B. 1972, *ApJ*, 175, L79
- Flannery, B. P. 1975, *MNRAS*, 170, 325
- Goodchild, S., & Ogilvie, G. 2006, *MNRAS*, 368, 1123
- Harry, G. M., & the LIGO Scientific Collaboration. 2010, *Classical and Quantum Gravity*, 27, 084006
- Harvey, D. A., Skillman, D. R., Kemp, J., et al. 1998, *ApJ*, 493, L105
- Hazboun, J. S., & Larson, S. L. 2013, *ArXiv e-prints*, arXiv:1311.3153
- Hils, D., Bender, P. L., & Webbink, R. F. 1990, *ApJ*, 360, 75
- Hut, P. 1981, *A&A*, 99, 126
- Kley, W., Papaloizou, J. C. B., & Ogilvie, G. I. 2008, *A&A*, 487, 671
- Larson, S. L. 2000, *Online Sensitivity Curve Generator*
- Larson, S. L., & Hiscock, W. A. 2000, *Phys. Rev. D*, 61, 104008
- Littenberg, T. B., Larson, S. L., Nelemans, G., & Cornish, N. J. 2013, *MNRAS*, 429, 2361
- Livas, J. e. a. 2012, SGO Mid A LISA-Like Concept for the Space-based Gravitational-wave Observatory (SGO) at a Middle Price-Point
- Lubow, S. H., & Shu, F. H. 1975, *ApJ*, 198, 383
- Lucy, L. B. 1967, *ZAp*, 65, 89
- Nelemans, G. 2010, LISA verification sources
- Nelemans, G., Portegies Zwart, S. F., Verbunt, F., & Yungelson, L. R. 2001a, *A&A*, 368, 939
- Nelemans, G., Yungelson, L. R., Portegies Zwart, S. F., & Verbunt, F. 2001b, *A&A*, 365, 491
- Orosz, J. A., & Bailyn, C. D. 1997, *ApJ*, 477, 876
- Paczynski, B. 1977, *ApJ*, 216, 822
- Patterson, J., Halpern, J., & Shambrook, A. 1993, *ApJ*, 419, 803
- Patterson, J., Sterner, E., Halpern, J. P., & Raymond, J. C. 1992, *ApJ*, 384, 234
- Peters, P. C. 1964, *Physical Review*, 136, 1224
- Peters, P. C., & Mathews, J. 1963, *Physical Review*, 131, 435
- Peterson, D. 1996, The Space Interferometry Mission, Tech. rep., Space Interferometry Science Working Group
- Ritter, H. 1980, *A&A*, 91, 161
- Roelofs, G. H. A., Groot, P. J., Nelemans, G., Marsh, T. R., & Steeghs, D. 2006, *MNRAS*, 371, 1231
- Sawada, K., & Matsuda, T. 1992, *MNRAS*, 255, 17P
- Solheim, J.-E., Provencal, J. L., Bradley, P. A., et al. 1998, *A&A*, 332, 939
- Stebbins, R. e. a. 2012, SGO High A LISA-Like Concept for the Space-based Gravitational-wave Observatory (SGO) at a High Price-Point
- Sulkanen, M. E., Brasure, L. W., & Patterson, J. 1981a, *ApJ*, 244, 579
- . 1981b, *ApJ*, 244, 579
- Timpano, S. E., Rubbo, L. J., & Cornish, N. J. 2006, *Phys. Rev. D*, 73, 122001
- von Zeipel, H. 1924, *MNRAS*, 84, 665
- Wahlquist, H. 1987, *General Relativity and Gravitation*, 19, 1101, 10.1007/BF00759146
- Wahlquist, H. 1987, *General Relativity and Gravitation*, 19, 1101

Warner, B. 1995, Ap&SS, 225, 249

Willems, B., Vecchio, A., & Kalogera, V. 2008,
Physical Review Letters, 100, 041102

Wilson, R. E., & Devinney, E. J. 1971, ApJ, 166,
605

December 8, 2014